ADVANCED OPTICAL MATERIALS
www.advopticalmat.de

# Large Non-Resonant Infrared Optical Second Harmonic Generation in Bulk Crystals of Van der Waals Semiconductor, $SnP_2Se_6$

*Jadupati Nag, Saugata Sarker, Safdar Imam, Abishek Iyer, Michael J. Waters, Albert Suceava, James M. Rondinelli, Mercouri G. Kanatzidis, and Venkatraman Gopalan**

**2D van der Waals (vdW) materials have emerged as a highly promising candidates for nonlinear optical (NLO) applications. This study presents the synthesis, comprehensive linear optical, and optical second harmonic generation (SHG) characterization of a novel 2D vdW semiconductor $SnP_2Se_6$ in its bulk single crystal form. It exhibits an indirect bandgap of ≈1.47 eV and an exceptional non-resonant SHG coefficient of $d_{33} \sim -222 \pm 30$ pm $V^{-1}$ at a fundamental wavelength of 2 µm, which is ≈7 times larger than that of the commercial $AgGaSe_2$ with a comparable bandgap. Density functional theory (DFT) calculations of the linear and nonlinear optical properties exhibit reasonable agreement with the experimental measurements, revealing the chemical origin of the enhanced properties. Moreover, $SnP_2Se_6$ can exhibit both type-I and type-II phase matching over a wide spectral range, fulfilling one of the key criteria for an ideal NLO crystal. These exceptional properties position $SnP_2Se_6$ as a highly promising candidate for NLO applications.**

## 1. Introduction

The advancement of nonlinear optics hinges on the discovery of new optical crystals with superior nonlinear optical (NLO) properties. Traditionally, materials such as $LiNbO_3$,[1] $AgGaSe_2$,[2] $\beta$-$BaB_2O_4$,[3] KDP,[4] $ZnGeP_2$,[5] GaSe,[6] and $BaTiO_3$[7] have been widely used. An ideal NLO crystal should possess key attributes, including a high nonlinear coefficient, a large laser-induced damage threshold (LIDT), a wide transparency range, a low extinction coefficient, phase-matching capability, and the ability to be grown into large, stable, high-quality single crystals.[8] In pursuit of designing new NLO crystals, dimensionality reduction offers a promising approach. For low-dimensional systems, such as 2D van der Waals (vdW) single crystals, reducing dimensionality can result in increased electronic polarizability and enhanced NLO properties.[9–12] 2D vdW materials can be exfoliated to produce ultra thin layers with precisely tunable optical properties, rendering them highly promising for multifunctional device applications.[13] Additionally, vdW materials are excellent candidates for NLO applications[14–18] due to their unique characteristics and adaptability, making them well-suited for advanced photonics,[19] optoelectronics,[20] laser technologies,[21] telecommunications,[22] and quantum computing.[23] To date, research efforts have primarily centered around graphene and transition metal dichalcogenides (TMDCs),[24–27] with relatively few studies on vdW crystals of metal chalcophosphates. Investigating additional 2D vdW materials could lead to the discovery of more efficient NLO materials.[28]

Our study examines a novel 2D layered vdW single crystal, $SnP_2Se_6$, aiming to identify its promising NLO properties through a combination of linear optical characterization (UV–vis, FTIR, spectroscopic ellipsometry), optical SHG measurements, and first-principles calculations. Recently, layer-dependent phenomena have been investigated in exfoliated atomically thin layers of $SnP_2Se_6$, focusing on applications in integrated photonics, photovoltaics, and related devices.[29,30] However, a thorough examination of the linear and nonlinear optical properties of bulk crystals are currently unexplored, including a full determination of the refractive index dispersion, its SHG tensor, as well as optical phase-matching conditions. The bulk crystals serve as a reference case to study intrinsic material properties in relation to those observed in atomically thin layers after exfoliation. Theory will further illustrate that the SHG coefficients are expected

J. Nag, S. Sarker, A. Suceava, V. Gopalan
Department of Materials Science and Engineering
Materials Research Institute
Pennsylvania State University
Millennium Science Complex Building
University Park, PA 16802, USA
E-mail: vxg8@psu.edu
S. Imam, A. Iyer, M. G. Kanatzidis
Department of Chemistry, Northwestern University
Evanston, IL 60208, USA
M. J. Waters, J. M. Rondinelli
Department of Materials Science and Engineering
Northwestern University
Evanston, IL 60208, USA

The ORCID identification number(s) for the author(s) of this article can be found under https://doi.org/10.1002/adom.202402649



**DOI: 10.1002/adom.202402649**

to decrease from the bulk to the monolayer limit, illustrating the importance of the vdW interactions.

In this work, we report the synthesis and detailed characterization of a novel 2D layered vdW semiconductor $SnP_2Se_6$. Large (≈ 6–10 mm), high-quality $SnP_2Se_6$ single crystals were successfully grown using Chemical Vapor Transport (CVT) with an optimized growth temperature profile and $SeCl_4$ as the transport agent for the first time. The optimized growth parameters enabled the growth of large crystals of $SnP_2Se_6$ with a suppressed phase of $Sn_2P_2Se_6$, a secondary phase commonly observed in earlier growth attempts.[30,31] Additionally, these crystals have demonstrated stable behavior in air and water over time as shown in Figure S2 (Supporting Information),[32] which presents the XRD patterns of the crystals after exposure to air and water for various durations. The high-quality crystals thus grown have facilitated a thorough characterization of their complete linear and NLO property tensors, which have not been determined before this study.

The $SnP_2Se_6$ bulk crystals exhibit a significant non-resonant SHG coefficient of $d_{33} = -222 \pm 30$ pm $V^{-1}$ at a fundamental wavelength of 2 µm, outperforming materials with similar bandgaps such as GaAs (130 pm $V^{-1}$),[33] $SnP_2S_6$ (53 pm $V^{-1}$),[34] and $AgGaSe_2$ (33 pm $V^{-1}$).[2] Previous studies on the similar vdW material $SnP_2S_6$[34] highlighted its potential as a mid-infrared NLO crystal, exhibiting phase-matchability and a significant nonresonant SHG response. Selenides generally have smaller bandgap and larger SHG coefficients than sulfides for the same family of compounds.[35–38] Indeed, the record for the largest non-resonant SHG coefficient is for the known NLO materials $\gamma$-$NaAsSe_2$[37] (with bandgap of 1.87 eV measured at a fundamental wavelength of 2 µm) and $\gamma$-$NaAs_{0.95}Sb_{0.05}Se_2$ (with bandgap of 1.78 eV measured at a fundamental wavelength of 3 µm).[38] In this spirit, we explore $SnP_2Se_6$ bulk crystals. We determined the complete index anisotropy and frequency dispersion, and show that these crystals should be type-I and type-II phase-matchable in the spectral range of 1–6 µm. Further, the first-principles theory provides insight into the electronic structure and second-order polarizability calculations, helping to elucidate how local chemical bonding contributes to the macroscopic SHG tensors. The calculated frequency-dependent second-order polarizabilities are in reasonable agreement with the experimentally measured SHG tensor values. These findings underscore $SnP_2Se_6$ as a promising candidate for nonlinear frequency conversion applications in the near and mid-infrared range.

## 2. Results and Discussion

### 2.1. Crystal Growth

Single crystals of $SnP_2Se_6$ were synthesized using a two-zone furnace's CVT method. Previous studies used stoichiometric amounts of elemental sources with $SnBr_4$ as the transport agent and growth temperatures set at 450°C on the source side and 325 °C on the sink side, resulting in the formation of both ternary phases $Sn_2P_2Se_6$ and $SnP_2Se_6$.[30,31] In our work, we pre-synthesized stoichiometric sources at 350 °C. $SeCl_4$ was used as a transport agent with the source material, and growth conditions were maintained at 380 °C on the source and 325 °C on the sink sides, producing large $SnP_2Se_6$ crystals. The crystals belong to space group $R3$ (#146) and exhibit a chiral, layered atomic arrangement, as depicted in **Figure 1a** with the lattice parameters $a = b = 6.3213(9)$Å and $c = 19.962(4)$Å. Within each layer, the P atoms are covalently bonded to one another and connect the P–Se sublayer, where the P-Se bonds display both covalent and ionic characteristics.

XRD analysis of the $SnP_2Se_6$ crystals and crystal powders synthesized via CVT method showed patterns (see Figure 1b) consistent with those previously reported in the literature. The XRD patterns confirm the high crystallinity of the samples, with a preferential orientation along the (00$l$) direction. Additional XRD measurements on various $SnP_2Se_6$ crystals, presented in Figure S1 (Supporting Information),[32] further confirmed these findings. A smaller value of full width at half-maximum (FWHM) indicates a higher crystalline quality of the single crystal.[38,39] The FWHM values of the (006) Bragg peak in all x-ray patterns were low (≲0.13°), indicating the higher crystalline quality of the $SnP_2Se_6$ CVT crystals. Furthermore, these crystals exhibit long-term stability in both air and water over time (see Figure S2 (Supporting Information)).[32] The as-grown larger (6–10 mm) $SnP_2Se_6$ crystals exhibit excellent uniformity, as depicted in the inset of Figure 1c.

### 2.2. Electronic Structure

Optical absorption spectroscopy conducted on the $SnP_2Se_6$ crystals indicates an indirect optical bandgap of 1.47 eV as shown in Figure 1c. From electronic band structure calculated with DFT (Figure 1d–f), $SnP_2Se_6$ exhibits an indirect bandgap of 0.65 eV with the valence band maximum (VBM) between the L and $B_1$ points and nearer to the latter. The under-prediction of the bandgap compared to the experimental bandgap is a well-known limitation of DFT.[40] The conduction band minimum is at the Γ point. Unusually, the lowest conduction band comprises one spin-paired band followed by another bandgap from 1.42 to 2.00 eV above the VBM. As shown in the projected density of states (PDOS) in Figure 1, the isolated lowest conduction band is associated with hybridization of the empty Sn-5s and Se-4p states. Above the second gap, bands comprise hybridized Se-4p and P-3$sp^3$ states. Substitution on the Sn sites, therefore, would provide an effective means to engineering the conduction band for tuning the linear and nonlinear optical properties. Upper valence bands are nearly pure Se-4p states with the lower valence bands showing moderate contributions from hybridization with P-3p and minor mixing with Sn-5p.

From the atomic structure, PDOS, and electron density, the nature of the chemical bonds becomes clearer. For Sn–Se bonds, the octahedral coordination of Sn and lack of hybridization between Sn and Se in the PDOS indicate that the Sn–Se bonds are almost entirely ionic. For Se–P bonds, the strong electron withdrawing of the Se atoms gives rise to $Se^{\frac{2}{3}-}$–like apical terminations and tetrahedral P-$sp^3$ rather than establishing bipyramidal geometry with a lone pair on the phosphorous. The lack of charge density between layers (marked by dotted lines), as seen in Figure 1f, and electron localization function (ELF), as seen in Figure S14 (Supporting Information),[32] supports the vdW nature of the interlayer bonding. To further support this, the interlayer bonding strength was computed by comparing the relaxed conventional cell and a relaxed monolayer in the conventional cell, without

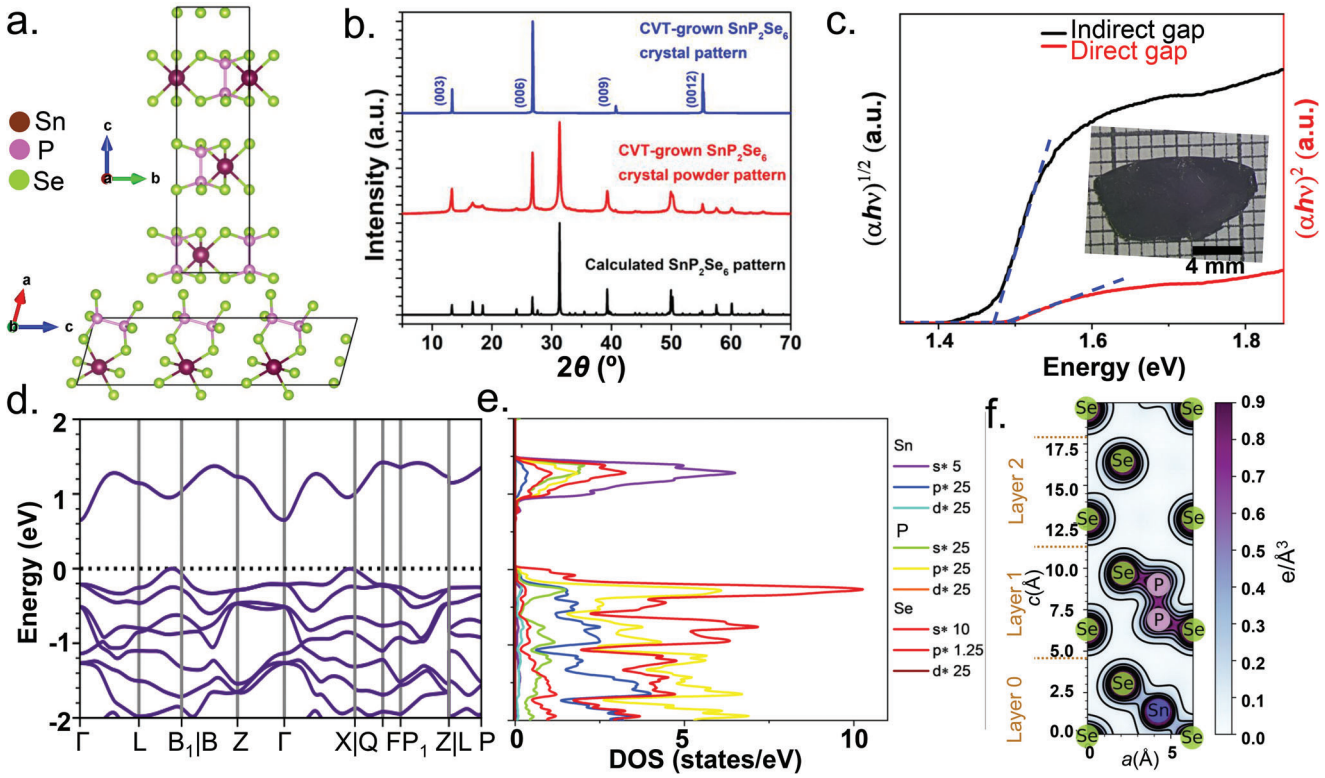


**Figure 1.** For $SnP_2Se_6$: a) crystal structure. The crystal structure comprises three identical layers with basal translations relative to each other. b) X-ray diffraction (XRD) patterns on CVT-grown crystal and crystalline powder. The calculated $SnP_2Se_6$ pattern was plotted to compare with the experimental patterns. The presence of sharp (00*l*) peaks in the single crystal XRD patterns indicates the high crystallinity of the CVT grown crystals. c) Tauc plots obtained from the UV–vis spectrum of a single crystal considering indirect and direct bandgaps. The inset displays an image of the grown single crystal. d) Band structure and e) Projected density of states (DOS) of $SnP_2Se_6$ in units of states per eV. f) A slice of the computed electron density passing through a pair of phosphorus atoms in the *a*-*c* plane. The interlayers are marked using dotted lines.

vdW corrections. We obtained a delamination energy of only 3.4 meV per atom, consistent with low stacking fault energies.

### 2.3. Crystal Domains

In 2D vdW materials, mismatches in layer stacking or twisting are frequently observed due to the weak van der Waals force between successive layers, a phenomenon known to influence their functional properties.[41,42] Our aim is to characterize the nonlinear optical susceptibility of this material in its bulk form, and given that second harmonic generation is sensitive to domains, we performed resonant SHG microscopy to identify the presence of domains in our bulk crystal. In SHG, the induced nonlinear polarization, $P^{2\omega}$, at frequency $2\omega$ (wavelength, $\lambda^{2\omega}$), and the incoming electric field $E^{\omega}$ of light at frequency $\omega$ (wavelength, $\lambda^{\omega}$), in a nonlinear optical material are related through the second-order optical susceptibility $P_i^{2\omega} = d_{ijk} E_j^{\omega} E_k^{\omega}$.[43] Here, the indices ($i$, $j$, $k$) denote the polarization directions in Cartesian coordinates. The SHG microscopy was performed at normal incidence (see **Figure** 2a) with fixed polarization conditions for the fundamental wavelength of $\lambda^{\omega} = 800$nm and the generated second harmonic light at $\lambda^{2\omega} = 400$nm detected; note that SHG wavelength of 400nm is resonant with an energy above the bandgap. This investigation reveals antipolar domains of two types: Domains related by a 2-fold rotation about the [01$\bar{1}$0] direction as seen in Figure 2b,c (we label these as type D1 domains), and domains where adjacent layers of the 2D vdW structure in the thickness direction could be related by spatial inversion, $\bar{1}$, as shown in Figure 2d,e (we label these as type D2 domains).

In domains of type D1, the contrast at the twin wall can be reversed by adjusting the polarization of the incident light as shown in Figure 2b. SHG polarimetry experiments (circles) and their modeling (solid line) help deduce that the slight relative rotation of the SHG polarimetry plots in the two regions (1 and 2 in Figure 2b) across the domain wall arises from a 180° rotation of the crystallographic axes about the [01$\bar{1}$0] direction. The crystal physics axes transforms cross the domain wall as ($Z_1$, $Z_2$, $Z_3$) → ($Z_1$, $-Z_2$, $-Z_3$), which then reverses the sign of $d_{22}$ and $d_{33}$ without reversing the sign of $d_{11}$. Laue backscattering and electron backscattering diffraction (EBSD) performed as described in Figures S6a and S7 (Supporting Information),[32] respectively, confirm the presence of these antipolar domains.

In domains of type D2 seen in Figure 2d, all the four regions indicated by the four locations 3–6 exhibit the same polar plots seen in Figure 2e; however their SHG intensities are different. These can occur if the adjacent 2D layers have crystal physics axes related by spatial inversion (crystal physics axes ($Z_1$, $Z_2$, $Z_3$) → ($-Z_1$, $-Z_2$, $-Z_3$), and hence $d_{ij} \rightarrow -d_{ij}$). This is schematically shown for six layers (as an example) below Figure 2d which can

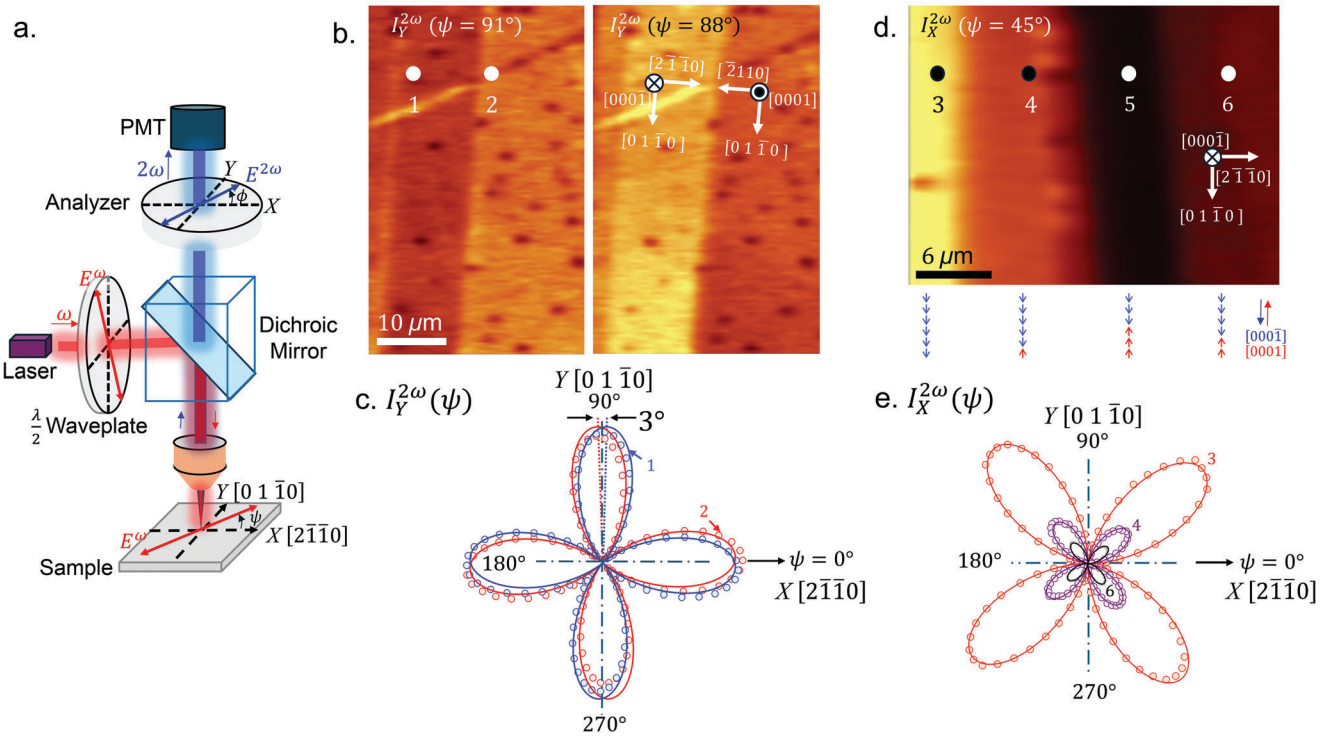


**Figure 2.** a) Experimental configuration of resonant SHG microscopy performed with $\lambda^{\omega} = 800$ nm fundamental light wavelength, generating an SHG of $\lambda^{2\omega} = 400$ nm. b) SHG microscopy imaging of 2-fold rotation domains in $SnP_2Se_6$ related by a 2-fold rotation about the [01$\bar{1}$0] direction. The right and left images demonstrate the domain contrast of the same region with two different incident polarization configurations as indicated in the images. c) SHG polarimetry (circles) and theory fitting (solid lines) at the locations 1 and 2 marked in panel (b) show a relative rotation that arises in point group *3* from a 180° rotation of the crystal axes about the [01$\bar{1}$0] axis across the domain wall as shown in panel (b). d) SHG microscopy of a different region on the crystal reveals bands of different intensities but identical polar plots in locations 3, 4, 6 as shown in panel e). Location 5 has such low SHG intensity that it is not seen on the scale plotted here. These are inversion domains whose crystal physics axes are related by $\bar{1}$ in different layers in the thickness direction as illustrated in the schematics below where the [000 ± 1] directions are shown in red (+) and blue (−) arrows for six example layers.

give rise to the four color contrasts that are seen. The SHG fields from type D2 antipolar layers will possess the same field amplitude but opposite phases. Upon averaging over the layers within the probe depth of the laser, a cross-cancellation of the fields between antipolar layers will yield a net field, and hence intensity, that is diminished relative to the case where all layers have the same polarity.

Both domain types, D1 and D2, discussed above, will influence the quantification of the SHG tensor. In domain type D1, the coefficients $d_{15} = d_{24}$, $d_{16} = d_{21} = -d_{22}$, $d_{31} = d_{32}$, $d_{33}$ would flip signs across domain walls. In domain type D2, all $d_{ij}$ would switch signs across domain walls. This will lead to partial cross-cancelation of the far-field SHG fields when averaged over domains and could lead to an underestimation of the SHG tensor, as is discussed further on.

### 2.4. Linear Optical Properties

Prior to measuring the nonlinear optical susceptibility in the bulk crystal, we first characterize its linear optical properties. The real and imaginary components of the refractive indices were determined using ellipsometry. There should be two distinct refractive indices for a material with space group *R*3: ordinary ($n_o$) and extraordinary ($n_e$) as shown in **Figure 3**a. $SnP_2Se_6$ exhibits a negative uniaxial behavior, namely, $n_o > n_e$. The birefringence of $SnP_2Se_6$ varied from 0.3 to 0.4 for photon energies lower than the bandgap. The experimental refractive indices beyond the band edge have been fitted with the Cauchy equation, $n(\lambda) = A + \frac{B}{\lambda^2} + \frac{C}{\lambda^4}$. Here, *A*, *B*, and *C* are constant fitting parameters, and the obtained values from the Cauchy fit are 2.43, 1.33 μm$^2$, 1.02 μm$^4$ for the ordinary index dispersion, and 2.15, 1.48 μm$^2$, 0.98 μm$^4$, for the extraordinary index dispersion.

The refractive indices calculated from first principles are in excellent agreement with experiments despite the independent particle approximation which typically overestimates the oscillator strengths and thus the dielectric function because the local field effects are not considered. The spectral features of the calculated refractive indices align in energy well with the experimental ones albeit with much sharper features due to a lack of broadening from finite temperature effects. The general alignment of the spectral features highlights the usefulness of scissor shift corrections in studying optical properties starting from computationally economical DFT calculations.

The NIR and MIR transparency window was measured using the UV–vis and FTIR spectroscopy as shown in Figure S4 (Supporting Information.)[32] The optical transparency window of this single crystal is from 1 μm to >16 μm in wavelength. When both the fundamental and SHG wavelengths are within the transparency range, optical absorption is minimized, and we term it a

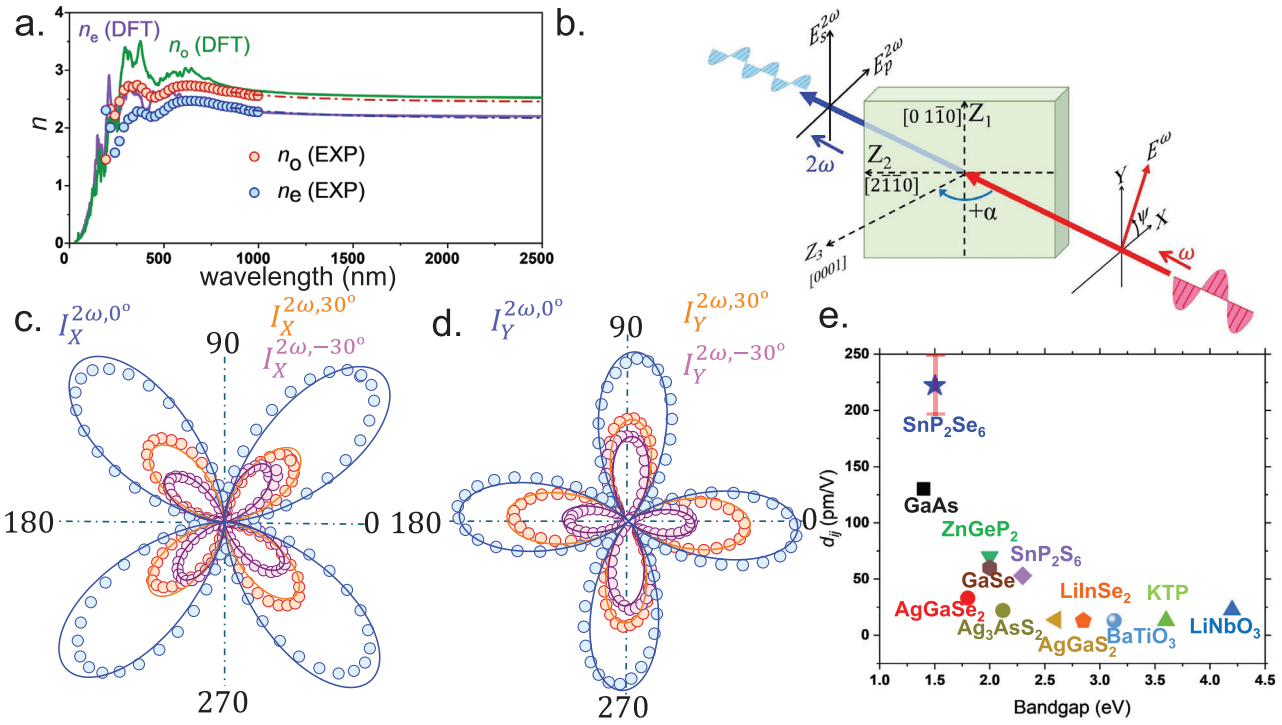


**Figure 3.** Linear and nonlinear optical properties of $SnP_2Se_6$: a) measured (red/blue circles) and DFT calculated (green/violet solid lines) ordinary ($n_o$) and extraordinary ($n_e$) refractive indices, along with the Cauchy fit (dashed-dotted curves) in the spectral range of 0.85–2.5 μm. b) Schematic of far-field SHG polarimetry experimental geometry for the non-resonant 2000 nm to 1000 nm SHG conversion. The crystallographic $Z_1$ ||$[01\bar{1}0]$ & $Z_2$ ||$[2\bar{1}\bar{1}0]$ were perpendicular to the crystal plane ($Z_3$ ||[0001]). Polarimetry plots of the SHG intensity as a function of the polarization of the incident light given by the polar angle, $\psi$, are shown in c) $I_X^{2\omega,\alpha}(\psi)$ for *s*-polarized SHG and d) $I_Y^{2\omega,\alpha}(\psi)$ for *p*-polarized SHG for three incidence angles of the fundamental light, namely, $\alpha = -30°$, 0°, 30°. The experimental data are shown as circles, while solid curves are theoretical fits based on point group *3*. e) A comparison of the SHG coefficients of $SnP_2Se_6$ with those of commercial NLO crystals measured at non-resonant pump wavelengths, see Table S2 (Supporting Information).[2,32,33,44–50] Error bar represents the standard deviation of SHG coefficient of $d_{33}$ for $SnP_2Se_6$ from the polarimetry fits for the non-resonant 2000 nm to 1000 nm SHG conversion.

non-resonant SHG measurement, which we proceed to describe next. If either or both of those wavelengths are outside this window, it is termed a resonant SHG measurement as shown earlier in Figure 2.

### 2.5. Optical Second Harmonic Generation (SHG)

Far-field SHG measurements were performed on single crystals of $SnP_2Se_6$ (thickness ≈125 μm) under non-resonant conditions to minimize the absorption at various incidence angles $\alpha$. Far-field geometry was used with a beam diameter of 50 μm; for quantitative analysis of the SHG coefficients, far-field allows for plane-wave approximation that is not valid for the high numerical aperture (NA) focused Gaussian beams of <1 μm diameter beams used in SHG microscopy in Figure 2. Far-field measurements also allow the collection of a larger number of independent sets of SHG polarimetry data at different incidence angles ($\alpha$ in Figure 3b) which is required to extract the complete SHG tensor. In contrast, the high NA objectives only allow for normal incidence and possess a complex polarization distribution across a Gaussian beam.

We used a fundamental wavelength of 2 μm, resulting in a SHG wavelength of 1 μm (see Figure 3b for a schematic of the SHG polarimetry experimental geometry), ensuring that the SHG is within the bandgap of 1.47 eV and is hence non-resonant. For comparison, a non-resonant fundamental at 1550 nm generating a resonant SHG at 775 nm was also measured. SHG polarimetry measurements were performed and analyzed to extract the SHG tensor of $SnP_2Se_6$ crystals. This is an alternative to performing Maker fringe measurements[51,52] where a sample tilt scan (varying $\alpha$ in Figure 2) is performed at a fixed polarization setting for the fundamental and the SHG waves; this works well for nearly perfect sample surfaces with planarity and parallelism. An alternate robust but equivalent method[51,52] works well, namely, by collecting a series of full SHG polarimetry data for a number of discrete incidence angles, and modeling them collectively to fit with a single set of SHG coefficients. By collecting a sufficient number of independent data sets, one can over-constrain the common fit and thus develop confidence in the fits. The second harmonic tensor for point group *3* is expressed in Voigt notation as:

$$d = \begin{pmatrix} d_{11} & -d_{11} & 0 & d_{14} & d_{15} & -d_{22} \\ -d_{22} & d_{22} & 0 & d_{15} & -d_{14} & -d_{11} \\ d_{31} & d_{31} & d_{33} & 0 & 0 & 0 \end{pmatrix} \quad (1)$$

**Table 1.** For $SnP_2Se_6$ single crystal, second-order NLO tensor from experiments at 2 and 1.55μm. Numbers within the parentheses are error bar representing the standard deviation of the SHG $d_{ij}$ coefficients. The presence of antiparallel domains might suggest that the $d_{31}$, $d_{33}$ and $d_{15}$ coefficients could be underestimated by up to ≈15 − 20%. A significant change in some of the ratios occurs between resonant (775 nm SHG) to non-resonant (1000 nm SHG) conditions.

| Ratio of $d_{ij}$ coefficients | Experimental ratios [1550 nm] | Experimental ratios [2000 nm] |
|---|---|---|
| $d_{11}/d_{22}$ | −7.9(0.9) | −12.9(0.8) |
| $d_{14}/d_{22}$ | −14(3.5) | 0.69(0.15) |
| $d_{15}/d_{22}$ | −54.2(18) | −20.2(2.0) |
| $d_{31}/d_{22}$ | 67.3(6) | 9.9(0.9) |
| $d_{33}/d_{22}$ | −280(67) | −222.0(30) |
| $d_{22}$ | −1.4(0.1) pm $V^{-1}$ | 1.0(0.1) pm $V^{-1}$ |

Here $d_{11}$, $d_{22}$, $d_{14}$, $d_{15}$, $d_{31}$ and $d_{33}$ are six non-zero SHG coefficients. The SHG intensity ($I^{2\omega}$) is expected to exhibit a quadratic dependence on the incident laser intensity ($I^{\omega}$). Experimentally, the dependence of SHG signal on fundamental power has been measured (see Figure S10, Supporting Information),[32] showing excellent agreement with the expected quadratic form $I^{2\omega} \propto (I^{\omega})^2$.

The results of SHG polarimetry at oblique incidences exhibit excellent agreement with the theoretical fit (Figure 3c,d). The ratios of the SHG coefficients $d_{ij}$ relative to $d_{22}$ were determined by concurrently fitting the polar plots at different incidence angles to an analytical model developed by Herman and Hayden[53] as implemented in the open-source #SHAARP software.[51,52] Note that in the Herman and Hayden model (built within the #SHAARP.ml code), multiple reflection of the ordinary and the extraordinary SHG waves are fully considered. These ratios are given in **Table 1**.

The absolute coefficients were also extracted by comparing the far-field SHG intensities at $\alpha = 0°$ for $SnP_2Se_6$ with those of a reference $z$-cut $LiNbO_3$ crystal, measured under identical experimental conditions (Figure S11, Supporting Information).[32] The full SHG tensor was determined for both the resonant regime (non-resonant excitation wavelength of 1550 nm leading to a resonant SHG at 775 nm, see Figure S9, Supporting Information)[32] and the non-resonant regime (non-resonant excitation wavelength of 2000 nm resulting in a non-resonant SHG at 1000 nm, see Figure 2) as summarized in Table 1. The measured non-resonant $d_{33} \approx -222$ pm $V^{-1}$ at a fundamental wavelength of 2 μm is remarkably high; it exceeds the benchmark infrared NLO crystals GaAs, $AgGaS_2$ and $AgGaSe_2$, $SnP_2S_6$ as shown in Figure 3e. For the resonant SHG at 775 nm generated by the 1550 nm fundamental light, the $d_{33}$ is even larger, namely, $d_{33} \approx +280$ pm $V^{-1}$ (and has a change in its sign); the sign change is consistent qualitatively with the DFT calculations as seen in **Figure** 4f; however, it is less useful for applications due to the accompanying larger linear optical absorption. In addition to the SHG polarimetry measurements and analysis described above, we also performed SHG Maker fringe measurements as described in Section 8(Supporting Information).[32] The results presented in Figure S12 (Supporting Information)[32] further confirm the SHG tensor given in Table 1.

Both type D1 and type D2 domains in Figure 2 can influence the magnitudes of the SHG tensors reported here. While an exact quantification of this underestimation is difficult, if we assume an average domain distribution over the entire far-field probe beam diameter of 50 μm that is similar to that in Figure 2d where the ratio of maximum SHG intensity to the average intensity is 2.19, then the maximum possible $d_{ij}$ would then be $\approx \sqrt{2.19} = 1.48\times$ the measured $d_{ij}$ listed in Table 1. Thus there could be an underestimation of the coefficients in Table 1 by ≈48%. Future quantification of the SHG tensor would require crystals with minimal domains and the ability to quantify local SHG polarimetry collected within small uniform domain regions by an SHG microscope using Gaussian beams with complex polarizations and with the ability to probe non-normal incidence waves using perhaps reflective objective.

Density functional theory was used to predict the frequency dispersion of the SHG coefficients as plotted in Figure 4a–f. The momentum-space dispersion of SHG contributions in the long wavelength limit for the conventional cell and a monolayer are shown in Figure S14 (Supporting Information);[32] the bulk theoretical spectra in Figure 4a–f are averaged over the Brillouin zone. Overall, the SHG coefficients calculated from first-principles are in reasonable agreement with the experimental values, being within a factor of two for most of the coefficients. For materials discovery this is usually sufficient to identify promising candidates, which is one of the goals of this work. However, the relatively large underestimation at 2 μm fundamental wavelength of the $d_{15}$ and $d_{33}$ at 3× and 3.7× smaller, respectively, than experiment suggests that the independent particle approximation is phenomenologically lacking. Our hypothesis is that the van der Waals layered structure of $SnP_2Se_6$ encourages planar confinement of excitonic states. In a fully connected material, Wannier excitons would be expected to delocalize more in the $c$-direction, which may explain why the $d_{33}$ coefficient is the most underpredicted. Unfortunately, including excitonic effects in ab initio calculations via the Bethe–Salpeter equation for linear optical properties comes with immense computational cost, which is further amplified by the finer Brillouin zone grids required for converged sampling of momentum-space dispersion of SHG contributions.[54–57]

It is known that in bulk semiconductors, excitonic states shift the oscillators to lower energies which increases the non-resonant SHG response.[58] Furthermore, there have been a number of experimental observations of large SHG responses from monolayers of 2D materials.[54,59,60] However, in the case of $SnP_2Se_6$, DFT predicts that the static SHG tensor elements ($d_{11}$, $d_{22}$, $d_{31}$) show a reduction in the magnitude from bulk to monolayer roughly in line with the expected 3× reduction from the lower density of states in Table S3 (Supporting Information)[32] and momentum-space dispersions. The reduction in $d_{33}$ from bulk to monolayer highlights the importance of inter-layer excitation despite weak ground state interactions.

### 2.6. Phase Matching

For efficient conversion from fundamental frequency to second harmonic frequency, the phase-matching condition is an important parameter to consider. In an ideal phase-matching

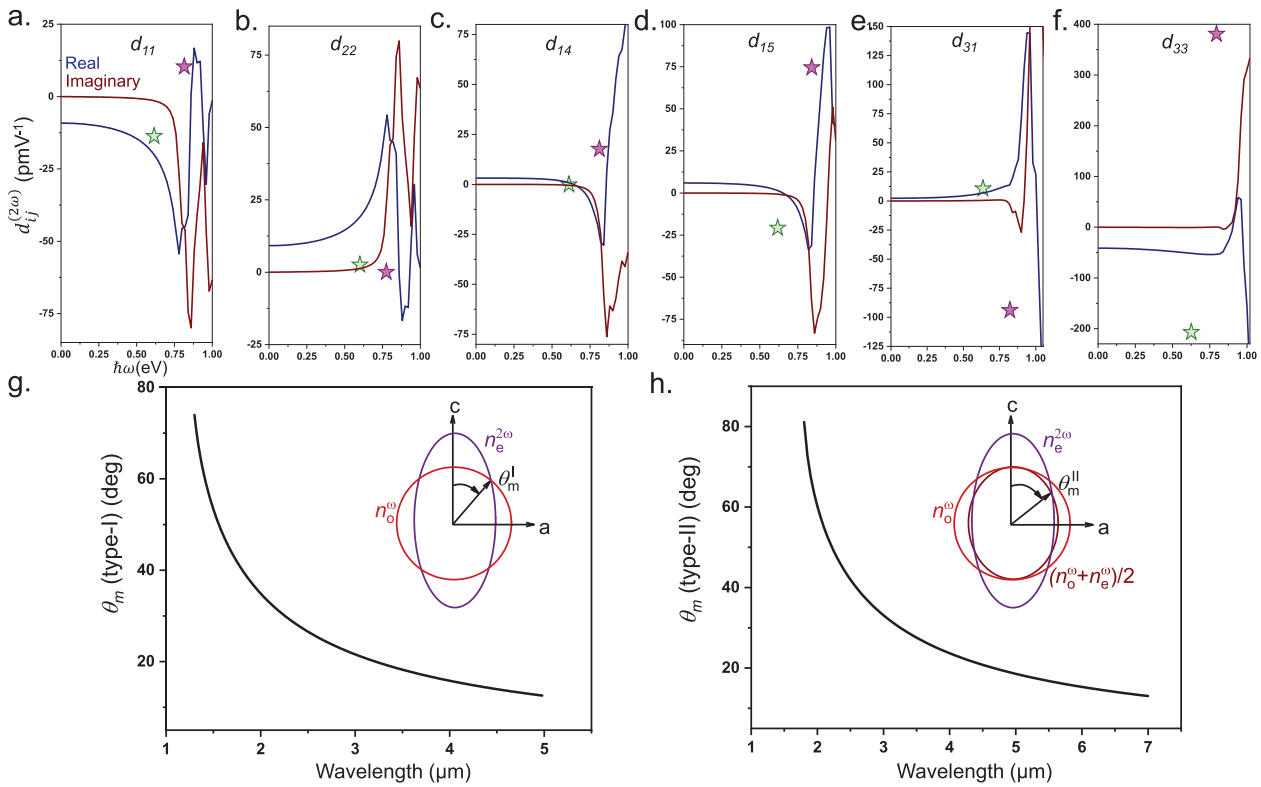


**Figure 4.** SHG coefficients and phase matching in $SnP_2Se_6$: a–f) the variation of complex SHG coefficients ($d_{ij}$) as a function of energy ($\hbar\omega$), calculated from first-principles theory. Experimental values of $|d_{ij}|$ coefficients are marked with a violet star ($\lambda^{\omega}$ = 1550 nm generating resonant SHG at $\lambda^{2\omega}$ = 775 nm) and green star (non-resonant $\lambda^{\omega}$ = 2000 nm generating non-resonant SHG at $\lambda^{2\omega}$ = 1000 nm). Phase-matching angles for type-I g) and type-II h) configurations are plotted as a function of the fundamental wavelength ($\lambda$). The insets illustrate the phase-matching angle in relation to the refractive index ellipsoids.

condition, the second harmonic wavevectors will interfere constructively with one another. Considering the single crystal as a parallel slab, interaction with the fundamental light at each point source should generate an SHG response. However, dispersion of the material will generally cause a phase difference between the second harmonic wave vector generated at each point source. Thus, the real part of the refractive indices at the fundamental and second harmonic wavelength should be equal to achieve a condition where the second harmonic light constructively interferes as it propagates through the crystal.[61]

For a birefringent crystal, there can be two types of phase matching methods, which are called type-I and type-II. The two generated SHG photons have the same polarization for type-I, whereas, in type-II phase matching, they have orthogonal polarizations. For a negative uniaxial material, the type-I phase matching can be achieved by measuring a phase-matching angle, $\theta_m$ defined with respect to the optic axis, which is parallel to crystallographic $c$ axis for $SnP_2Se_6$ (Figure 4g.). To achieve type-I phase matching, a negative uniaxial crystal satisfies the condition of $n_o^{\omega} = n_e^{2\omega}(\theta_m)$. For type-II phase-matching, the condition to satisfy is $n_o^{\omega} + n_e^{\omega}(\theta_m) = 2n_e^{2\omega}(\theta_m)$. The refractive indices were fitted with the Cauchy relationship, the energy range starting from the band edge. Considering the Cauchy model, the phase-matching angle was calculated for both type-I and type-II conditions (Figure 4g,h). This investigation shows the potential possibility of type-I and type-II phase matching for these single crystals in the non-resonant IR range. The phase-matchability of $SnP_2Se_6$ single crystal could facilitate its utilization in optical parametric amplifiers (OPA).[62]

### 2.7. Laser Damage and Thermal stability

The laser-induced surface damage threshold (LISDT) has been measured for the $SnP_2Se_6$ single crystal by exposing the sample at different incident fluences with a 1 MHz 100 fs laser with a 2000 nm wavelength. We have observed the sample under the optical microscope after irradiating under different fluences for 1 min. The optical microscopy images before and after the sample damage at the lowest possible fluence are shown in Figure S8a,b (Supporting Information).[32] Based on this, we have calculated the LISDT of this single crystal to be 35±5 GW cm$^{-2}$. With appropriate surface antireflection coatings, the damage threshold could potentially be higher. Thermogravimetric analysis (TGA) measurement (Figure S5, Supporting Information)[32] indicates that the highest operating temperature without thermal degradation is 350°C.

## 3. Conclusion

In summary, the novel 2D vdW semiconductor $SnP_2Se_6$ in its bulk single crystal form exhibits an extraordinarily high

non-resonant second-order nonlinear SHG coefficient of $d_{33}$ = −222±30 pm $V^{-1}$ at a fundamental wavelength of 2000 nm, which is ≈ 7 × greater than that of the commercially available NLO material $AgGaSe_2$, with a similar bandgap. The full SHG tensor has been quantitatively determined, noting that the presence of antipolar domains might have further led to an underestimation of the SHG tensor reported here. The first principles calculations provide insights into the electronic and structural properties, and are in reasonable agreement with the experimental SHG coefficient measurements. Furthermore, $SnP_2Se_6$ is capable of both type-I and type-II phase matching across a broad spectral range, and a high laser-induced surface damage threshold. These outstanding properties highlight $SnP_2Se_6$ to be a highly promising nonlinear optical crystal.

## 4. Experimental Section

*Synthesis*: The following reagents were utilized in their as-received states: tin powder (Sn, 4N purity, American Elements), phosphorus powder (P, 4N purity, Sigma–Aldrich), selenium shot (Se, 5N purity, Sigma–Aldrich), and selenium tetrachloride ($SeCl_4$, Sigma–Aldrich). Phosphorus and selenium were loaded in their stoichiometric ratio to prepare $P_2Se_5$ into a fused silica tube with 14 mm and 18 mm inner and outer diameters, respectively. Subsequently, the tube was sealed under a vacuum of $3.2 \times 10^{-3}$ mbar using an oxy/natural gas torch. The tube was loaded into a computer-controlled furnace, gradually heated to 500 °C over 18 h, held at this temperature for 72 h, and then cooled to room temperature over 8 h. Further, Sn, Se, and as-synthesized $P_2Se_5$ were loaded in their stoichiometric ratio to pre-synthesize $SnP_2Se_6$ into a fused silica tube with 14 and 18 mm inner and outer diameters, respectively. Subsequently, the tube was sealed under a vacuum of $3.2 \times 10^{-3}$ mbar using an oxy/natural gas torch. The tube was loaded into a computer-controlled furnace, gradually heated to 350 °C over 12 h, held at this temperature for 24 h, and then cooled to room temperature over 8 h.

*$SnP_2Se_6$ Crystal Growth*: $SnP_2Se_6$ crystals were grown using the Chemical Vapor Transport (CVT) method in a two-zone furnace. Pre-synthesized polycrystalline $SnP_2Se_6$ materials (2 g) were initially combined with transport agent $SeCl_4$ (30 mg) and loaded into a fused silica tube with 16 mm and 18 mm inner and outer diameters, respectively, and a length of 30 cm. The mixture was sealed under vacuum conditions using an oxy/natural gas torch. The CVT growth process involved two temperature zones: *Source Zone (380 °C)*: The mixture was placed in this zone. Over 12 h, the temperature was gradually increased to 325 °C and held there for 12 h. Subsequently, it was heated to 380 °C over 3 h and maintained for 170 h. Finally, the temperature was reduced to ambient levels over 6 h. *Deposition Zone (325 °C)*: $SnP_2Se_6$ crystals obtained in this zone. The heating process followed a similar pattern: 12 h to 380 °C, 12 h holding time, 3 h to 325 °C, 170 h holding time, and cooling to ambient temperature over 6 h. Notably, these $SnP_2Se_6$ crystals were characterized directly without any further processing steps. The resulting crystals exhibit uniform surface morphology, making them suitable for NLO-SHG measurements.

*Crystal Structure Characterization*: X-ray diffraction (XRD) patterns of CVT crystals and crystal powder were obtained using a Rigaku Miniflex600 X-ray diffraction system equipped with a Dtex silicon 1-D detector. The Cu K$\alpha$ radiation (wavelength $\lambda$ = 1.5406 Å) was generated by applying a voltage of 40 kV and a current of 15 mA. The radiation was filtered with a graphite -monochromator and a K$\beta$ foil filter. A zero-background silicon holder was used for the measurements. The UV–vis–NIR spectrum (shown as Tauc plots) in transmittance mode was collected at room temperature using a $SnP_2Se_6$ crystal on a Cary 5000 UV–vis–NIR double-beam spectrophotometer with a monochromator. An empty substrate was used as the reference for the baseline measurement.

*Linear Optical Properties*: The linear optical properties of $SnP_2Se_6$ single crystals were investigated using UV–vis spectroscopy (Agilent UV-VIS-NIR Spectrophotometer) and Fourier transform infrared (FTIR) spectroscopy (Bruker Vortex 80 with HgCdTe detector) across the spectral ranges of 0.25–2 and 2–16 µm, respectively. Both spectroscopic measurements were conducted by mounting the single crystal samples facing the crystallographic *c* direction toward the beam on to the integrating sphere in transmission and reflection geometries. In FTIR, the data was compared with the reference spectrum in the air (for transmission) and gold (for reflection). Ellipsometry measurements were conducted to determine the real and imaginary parts of the refractive index (*n* and *k*) within the 0.2–1 µm spectral range. Data were collected in two sample configurations, with the optic axis oriented both parallel and perpendicular to the plane of incidence. The data were simultaneously fitted to extract the corresponding oscillators, allowing the determination of *n* and *k* from the experimental parameters. Additionally, the ordinary ($n_o$) and extraordinary ($n_e$) refractive indices were derived from the two experimental geometries.

*SHG Polarimetry*: SHG is a nonlinear optical process in which two photons at a fundamental frequency ($\omega$) combine to produce a photon with double the frequency ($2\omega$). In a nonlinear optical material, the induced nonlinear polarization, $P^{2\omega}$, at frequency $2\omega$, is related to the incident electric field, $E^{\omega}$, at frequency $\omega$, through the second-order optical susceptibility $P_i^{2\omega} = d_{ijk} E_j^{\omega} E_k^{\omega}$.[43] Here, the indices ($i, j, k$) represent the polarization directions in Cartesian coordinates. SHG experiments were performed using transmission geometry with a 2000 nm fundamental laser beam (Spirit Nopa, 100 fs, 1 MHz). The measurements were performed in transmission geometry under normal and oblique incidences. The transmitted SHG field was then split into p-polarized (X) and s-polarized (Y) components using an analyzer and detected using a photomultiplier tube. In the experimental geometry, SHG polarimetry was measured in two conditions where crystallographic $Z_1 \| [01\bar{1}0]$ and $Z_2 \| [2\bar{1}\bar{1}0]$ were perpendicular to the plane of incidence ($Z_3 \| [0001]$). For SHG polarimetry, the nonlinear optical intensity was measured as a function of the incidence angle of the linearly polarized light ($E^{\omega} = (E^{\omega}\cos\psi, E^{\omega}\sin\psi, 0)$,). To determine the NLO coefficients, an SHG polarimetry experiment was conducted, with the results subsequently fitted and analyzed using the open-source #SHAARP software.[51,52]

*SHG Microscopy*: The SHG microscopy measurements were performed in reflection geometry in normal incidence with an 800 nm fundamental laser beam (Spectra-Physics Ti: sapphire source 80 fs, 80 MHz). A dichroic mirror separates light at $2\omega$ from the fundamental beam ($\omega$). The objective of the microscope had a numerical aperture of 0.40.

*First Principles Calculations*: Theoretical calculations were performed within the ab initio software package GPAW[63,64] (version 24.7.0b1-252d1fd11a). First, ground state calculations were performed using Density Functional Theory (DFT) with the Perdew–Burke–Ernzerhof[65] (PBE) functional and its corresponding pseudopotential set included with GPAW (v0.9.20000). The Atomic Simulation Environment[66] (ASE) (version 3.23.1b1-411c521370) was used for calculation workflow automation, creation of band structures, and plotting of band paths in the Brillouin zone (BZ). DFT calculations were performed with a planewave cut-off of 600 eV, an augmentation grid with 2X the linear density of the planewave grid, Γ-centered *k*-point grids, and with an electronic eigenvalue convergence criterion of $10^{-7}$ eV.

For ground state self-consistent (SCF) calculations, an additional charge density convergence criterion of $10^{-5}$ electrons per valence electron was enforced. The rhombohedral primitive cell ($a = b = c = 7.58916$, $\alpha = \beta = \gamma = 49.2237°$) containing one formula unit of $SnP_2Se_6$ was cut from experimentally determined hexagonal conventional cell for ab initio calculations. Ground state SCF calculations were performed with an 8 × 8 × 8 *k*-grid. Atomic orbital projected density of states calculations and optical properties calculations were performed starting from non-self-consistent (NSCF) calculations, where the linear *k*-grid density was doubled for a 16 × 16 × 16 *k*-grid. Relaxations were terminated when no forces exceeded 5 meV/Å.

The high-symmetry *k*-path through the BZ used for the NSCF electronic band structure calculation follows the AFLOW standard.[67] For optical properties, the NSCF calculations were performed ensuring convergence of bands 40 eV above the conduction band minimum, requiring 6× the number of bands in the ground state calculations. Calculation of

the frequency-dependent response spectra, the dielectric and SHG tensors, were performed within the length-gauge[54,68] using the independent particle approximation (i.e. sum-over-bands approach) with an oscillator smearing ($\eta$) of 20 meV. To ensure only converged bands were included in the summation, the summation was limited to a maximum frequency of 40 eV. A scissor shift of 0.85 eV was applied to correct for the bandgap under-prediction by DFT. The response spectra at each of the *k*-points in the fine BZ grid were computed independently and subsequently averaged to obtain the bulk values. Since the response spectra can be computed independently for each *k*-point, the *k*-space dependence SHG contributions was visualized by plotting the static ($\omega \rightarrow 0$) second order polarizability, $\chi^{(2)}_{ijk}$, along the high-symmetry path normally used for the electronic band structures.

## Supporting Information

Supporting Information is available from the Wiley Online Library or from the author.

## Acknowledgements

J.N., S.S., and S.I. contributed equally to this work. This work was supported by the Air Force Office of Scientific Research through the Grant award number FA 9550-23-1-0658. S.S. and V.G. acknowledge the National Science Foundation Grant Number DMR-2210933. A.S. was supported by the Center for 3D Ferroelectric Microelectronics (3DFeM), an Energy Frontier Research Center funded by the U.S. Department of Energy, Office of Science, Office of Basic Energy Sciences Energy Frontier Research Centers program under Award Number DE-SC0021118. The computational work used resources of the National Energy Research Scientific Computing Center (NERSC), a DOE Office of Science User Facility supported by the Office of Science of the U.S. Department of Energy under Contract No. DE-AC02 -05CH11231 using NERSC award BES-ERCAP0028012 (2024).

## Conflict of Interest

The authors declare no conflict of interest.

## Data Availability Statement

The data that support the findings of this study are available from the corresponding author upon reasonable request.

## Keywords

infrared nonlinear optical crystals, nonlinear optics, second harmonic generation, van der Waals material

Received: October 7, 2024
Revised: February 16, 2025
Published online: March 7, 2025

[1] R. C. Miller, W. A. Nordland, P. M. Bridenbaugh, *J. Appl. Phys.* **1971**, *42*, 4145.
[2] H. Kildal, J. Mikkelsen, *Opt. Commun.* **1973**, *9*, 315.
[3] R. Ganeev, I. Kulagin, A. Ryasnyansky, R. Tugushev, T. Usmanov, *Opt. Commun.* **2004**, *229*, 403.
[4] Z. Lin, Z. Wang, C. Chen, M.-H. Lee, *J. Chem. Phys.* **2003**, *118*, 2349.
[5] G. Boyd, E. Buehler, F. Storz, *Appl. Phys. Lett.* **1971**, *18*, 301.
[6] K. R. Allakhverdiev, M. Ö. Yetis, S. Özbek, T. K. Baykara, E. Y. Salaev, *Laser Phys.* **2009**, *19*, 1092.
[7] S. Al-Ithawi, W. A. Hekmat, K. A. Hubeatir, S. Basil Ali, S. M. Kadhim, M. S. Hamza, *Mater. Sci. Forum* **2020**, *1002*, 132.
[8] M.-Y. Ran, A.-Y. Wang, W.-B. Wei, X.-T. Wu, H. Lin, Q.-L. Zhu, *Coord. Chem. Rev.* **2023**, *481*, 215059.
[9] Q. Wu, C. Yang, X. Liu, J. Ma, F. Liang, Y. Du, *Mater. Today Phys.* **2021**, *21*, 100569.
[10] J.-H. Song, A. J. Freeman, T. K. Bera, I. Chung, M. G. Kanatzidis, *Phys. Rev. B* **2009**, *79*, 245203.
[11] I. Chung, M. G. Kanatzidis, *Chem. Mater.* **2014**, *26*, 849.
[12] T. K. Bera, J.-H. Song, A. J. Freeman, J. I. Jang, J. B. Ketterson, M. G. Kanatzidis, *Angew. Chem., Int. Ed.* **2008**, *47*, 7828.
[13] X. Zeng, C. Wan, Z. Zhao, D. Huang, Z. Wang, X. Cheng, T. Jiang, *Front. Phys.* **2023**, *19*, 33301.
[14] A. Autere, H. Jussila, Y. Dai, Y. Wang, H. Lipsanen, Z. Sun, *Adv. Mater.* **2018**, *30*, 1705963.
[15] S. Ahmed, X. Jiang, C. Wang, U. e. Kalsoom, B. Wang, J. Khan, Y. Muhammad, Y. Duan, H. Zhu, X. Ren, H. Zhang, *Adv. Opt. Mater.* **2021**, *9*, 2001671.
[16] P. Yin, X. Jiang, R. Huang, X. Wang, Y. Ge, C. Ma, H. Zhang, *Adv. Mater. Interfaces* **2021**, *8*, 2100367.
[17] B. Guo, Q.-l. Xiao, S.-h. Wang, H. Zhang, *Laser Photonics Rev.* **2019**, *13*, 1800327.
[18] W. Liu, M. Liu, X. Liu, X. Wang, H.-X. Deng, M. Lei, Z. Wei, Z. Wei, *Adv. Opt. Mater.* **2020**, *8*, 1901631.
[19] H. Ling, R. Li, A. R. Davoyan, *ACS Photonics* **2021**, *8*, 721.
[20] X. Zhou, X. Hu, J. Yu, S. Liu, Z. Shu, Q. Zhang, H. Li, Y. Ma, H. Xu, T. Zhai, *Adv. Funct. Mater.* **2018**, *28*, 1706587.
[21] J. He, C. Wang, B. Zhou, Y. Zhao, L. Tao, H. Zhang, *Mater. Horiz.* **2020**, *7*, 2903.
[22] H. Yu, Z. Cao, Z. Zhang, X. Zhang, Y. Zhang, *Int. J. Miner. Metall. Mater.* **2022**, *29*, 671.
[23] S. Jenkins, L. Rózsa, U. Atxitia, R. F. L. Evans, K. S. Novoselov, E. J. G. Santos, *Nat. Commun.* **2022**, *13*, 6917.
[24] S. D. Lawaniya, S. Kumar, Y. Yu, H.-G. Rubahn, Y. K. Mishra, K. Awasthi, *Mater. Today Chem.* **2023**, *29*, 101428.
[25] X. Li, L. Wu, L. Hao, Y. Fu, in *Emerging Materials for Energy Conversion and Storage*, (Eds.: K. Y. Cheong, G. Impellizzeri, M. A. Fraga), Elsevier, Amsterdam **2018**, pp. 155–183.
[26] W. Li, Y. Huang, Y. Liu, M. C. Tekell, D. E. Fan, *Nano Today* **2019**, *29*, 100799.
[27] R. Ma, D. S. Sutherland, Y. Shi, *Mater. Today* **2021**, *50*, 570.
[28] C. He, Q. Zhao, Y. Huang, L. Zhu, S. Zhang, J. Bai, X. Xu, *J. Phys. Chem. Lett.* **2019**, *10*, 2090.
[29] C.-Y. Zhu, Z. Zhang, J.-K. Qin, Z. Wang, C. Wang, P. Miao, Y. Liu, P.-Y. Huang, Y. Zhang, K. Xu, L. Zhen, Y. Chai, C.-Y. Xu, *Nat. Commun.* **2023**, *14*, 2521.
[30] V. K. Sangwan, D. G. Chica, T.-C. Chu, M. Cheng, M. A. Quintero, S. Hao, C. E. Mead, H. Choi, R. Zu, J. Sheoran, J. He, Y. Liu, E. Qian, C. C. Laing, M.-A. Kang, V. Gopalan, C. Wolverton, V. P. Dravid, L. J. Lauhon, M. C. Hersam, M. G. Kanatzidis, *Sci. Adv.* **2024**, *10*, eado8272.
[31] D. Chica, V. Sangwan, *Res. square* **2022**.
[32] *See the Supplementary material for auxiliary information on "Large non-resonant infrared optical second harmonic generation in bulk crystals of van der Waals Semiconductor, $SnP_2Se_6$"* **2024**.
[33] T. Skauli, K. L. Vodopyanov, T. J. Pinguet, A. Schober, O. Levi, L. A. Eyres, M. M. Fejer, J. S. Harris, B. Gerard, L. Becouarn, E. Lallier, G. Arisholm, *Opt. Lett.* **2002**, *27*, 628.
[34] J. He, S. H. Lee, F. Naccarato, G. Brunin, R. Zu, Y. Wang, L. Miao, H. Wang, N. Alem, G. Hautier, G.-M. Rignanese, Z. Mao, V. Gopalan, *ACS Photonics* **2022**, *9*, 1724.
[35] I. Chung, M. G. Kanatzidis, *Chem. Mater.* **2014**, *26*, 849.

[36] L. Kang, M. Zhou, J. Yao, Z. Lin, Y. Wu, C. Chen, *J. Am. Chem. Soc.* **2015**, *137*, 13049.
[37] J. He, A. K. Iyer, M. J. Waters, S. Sarkar, R. Zu, J. M. Rondinelli, M. G. Kanatzidis, V. Gopalan, *Adv. Opt. Mater.* **2022**, *10*, 2101729.
[38] A. K. Iyer, J. He, H. Xie, D. Goodling, D.-Y. Chung, V. Gopalan, M. G. Kanatzidis, *Adv. Funct. Mater.* **2023**, *33*, 2211969.
[39] X. Zhang, J. Kang, K. H. Choi, J. Jeon, B. J. Jeong, H.-S. Bang, H.-S. Oh, J. Lim, J.-H. Park, J.-H. Lee, H. K. Yu, J.-Y. Choi, *Chem. Mater.* **2024**, *36*, 2533.
[40] J. P. Perdew, *Int. J. Quantum Chem.* **1985**, *28*, 497.
[41] M. Jang, S. Lee, F. Cantos-Prieto, I. Košić, Y. Li, A. R. C. McCray, M.-H. Jung, J.-Y. Yoon, L. Boddapati, F. L. Deepak, H. Y. Jeong, C. M. Phatak, E. J. G. Santos, E. Navarro-Moratalla, K. Kim, *Nat. Commun.* **2024**, *15*, 5925.
[42] X. Shi, Y. Kurman, M. Shentcis, L. J. Wong, F. J. García de Abajo, I. Kaminer, *Light: Science & Applications* **2023**, *12*, 148.
[43] S. A. Denev, T. T. A. Lummen, E. Barnes, A. Kumar, V. Gopalan, *J Amer. Cer. Soc.* **2011**, *94*, 2699.
[44] Y. Tang, K. C. Mandal, J. A. McGuire, C. W. Lai, *Phys. Rev. B* **2016**, *94*, 125302.
[45] H. Wu, Z. Wang, Y. Ni, M. Mao, C. Huang, X. Cheng, *J. Cryst. Growth* **2012**, *353*, 158.
[46] J. Zhou, W. Zhang, M. Liu, P. T. Lin, *Photon. Res.* **2019**, *7*, 1193.
[47] J.-J. Zondy, D. Touahri, O. Acef, *J. Opt. Soc. Am. B* **1997**, *14*, 2481.
[48] G. Boyd, H. Kasper, J. McFee, *IEEE J. Quantum Electron.* **1971**, *7*, 563.
[49] L. Isaenko, A. Yelisseyev, S. Lobanov, V. Petrov, F. Rotermund, G. Slekys, J.-J. Zondy, *J. Appl. Phys.* **2002**, *91*, 9475.
[50] R. Eckardt, H. Masuda, Y. Fan, R. Byer, *IEEE J. Quantum Electron.* **1990**, *26*, 922.
[51] R. Zu, B. Wang, J. He, J.-J. Wang, L. Weber, L.-Q. Chen, V. Gopalan, *npj Comput. Mater.* **2022**, *8*, 246.
[52] R. Zu, B. Wang, J. He, L. Weber, A. Saha, L.-Q. Chen, V. Gopalan, *npj Comput. Mater.* **2024**, *10*, 64.
[53] W. N. Herman, L. M. Hayden, *J. Opt. Soc. Am. B* **1995**, *12*, 416.
[54] A. Taghizadeh, K. S. Thygesen, T. G. Pedersen, *ACS Nano* **2021**, *15*, 7155.
[55] D. Y. Qiu, F. H. da Jornada, S. G. Louie, *Phys. Rev. Lett.* **2013**, *111*, 216805.
[56] K. S. Thygesen, *2D Mater.* **2017**, *4*, 022004.
[57] A. Riefer, W. G. Schmidt, *Phys. Rev. B* **2017**, *96*, 235206.
[58] T. G. Pedersen, H. D. Cornean, *Europhys. Lett.* **2007**, *78*, 27005.
[59] J. Zhang, W. Zhao, P. Yu, G. Yang, Z. Liu, *2D Mater.* **2020**, *7*, 042002.
[60] H. Wang, X. Qian, *Nano Lett.* **2017**, *17*, 5027.
[61] W. Zhang, H. Yu, H. Wu, P. S. Halasyamani, *Chem. Mater.* **2017**, *29*, 2655.
[62] G. Cerullo, S. De Silvestri, *Rev. Sci. Instrum.* **2003**, *74*, 1.
[63] J. Enkovaara, C. Rostgaard, J. J. Mortensen, J. Chen, M. Dułak, L. Ferrighi, J. Gavnholt, C. Glinsvad, V. Haikola, H. A. Hansen, H. H. Kristoffersen, M. Kuisma, A. H. Larsen, L. Lehtovaara, M. Ljungberg, O. Lopez-Acevedo, P. G. Moses, J. Ojanen, T. Olsen, V. Petzold, N. A. Romero, J. Stausholm-Møller, M. Strange, G. A. Tritsaris, M. Vanin, M. Walter, B. Hammer, H. Häkkinen, G. K. H. Madsen, R. M. Nieminen, et al., *J. Phys.: Condens. Matter* **2010**, *22*, 253202.
[64] J. J. Mortensen, L. B. Hansen, K. W. Jacobsen, *Phys. Rev. B* **2005**, *71*, 035109.
[65] J. P. Perdew, K. Burke, M. Ernzerhof, *Phys. Rev. Lett.* **1996**, *77*, 3865.
[66] A. H. Larsen, J. J. Mortensen, J. Blomqvist, I. E. Castelli, R. Christensen, M. Dułak, J. Friis, M. N. Groves, B. Hammer, C. Hargus, E. D. Hermes, P. C. Jennings, P. B. Jensen, J. Kermode, J. R. Kitchin, E. L. Kolsbjerg, J. Kubal, K. Kaasbjerg, S. Lysgaard, J. B. Maronsson, T. Maxson, T. Olsen, L. Pastewka, A. Peterson, C. Rostgaard, J. Schiøtz, O. Schütt, M. Strange, K. S. Thygesen, T. Vegge, et al., *J. Phys.: Condens. Matter* **2017**, *29*, 273002.
[67] W. Setyawan, S. Curtarolo, *Comput. Mater. Sci.* **2010**, *49*, 299.
[68] J. E. Sipe, A. I. Shkrebtii, *Phys. Rev. B* **2000**, *61*, 5337.